

Provided for non-commercial research and education use.
Not for reproduction, distribution or commercial use.



(This is a sample cover image for this issue. The actual cover is not yet available at this time.)

This article appeared in a journal published by Elsevier. The attached copy is furnished to the author for internal non-commercial research and education use, including for instruction at the authors institution and sharing with colleagues.

Other uses, including reproduction and distribution, or selling or licensing copies, or posting to personal, institutional or third party websites are prohibited.

In most cases authors are permitted to post their version of the article (e.g. in Word or Tex form) to their personal website or institutional repository. Authors requiring further information regarding Elsevier's archiving and manuscript policies are encouraged to visit:

<http://www.elsevier.com/copyright>

Available online at www.sciencedirect.com

SciVerse ScienceDirect

journal homepage: www.elsevier.com/locate/jmbbm

Research Paper

Identifying the dynamic compressive stiffness of a prospective biomimetic elastomer by an inverse method

Steven P. Mates^{a,*}, Aaron M. Forster^a, Donald Hunston^a, Richard Rhorer^a,
Richard K. Everett^b, Kirth E. Simmonds^c, Amit Bagchi^b

^aNational Institute of Standards and Technology, 100 Bureau Drive, Stop 8553, Gaithersburg, Maryland 20899, United States

^bNaval Research Laboratory, 4555 Overlook Ave SW, Washington, DC 20375, United States

^cScience Applications International Corporation, Washington, DC, United States

ARTICLE INFO

Article history:

Received 23 November 2011

Received in revised form

23 April 2012

Accepted 30 April 2012

Available online 14 May 2012

Keywords:

Biomimetic material

Kolsky bar

High-strain-rate

Digital image correlation

Inverse problem

Finite element analysis

ABSTRACT

Soft elastomeric materials that mimic real soft human tissues are sought to provide realistic experimental devices to simulate the human body's response to blast loading to aid the development of more effective protective equipment. The dynamic mechanical behavior of these materials is often measured using a Kolsky bar because it can achieve both the high strain rates ($> 100 \text{ s}^{-1}$) and the large strains ($> 20\%$) that prevail in blast scenarios. Obtaining valid results is challenging, however, due to poor dynamic equilibrium, friction, and inertial effects. To avoid these difficulties, an inverse method was employed to determine the dynamic response of a soft, prospective biomimetic elastomer using Kolsky bar tests coupled with high-speed 3D digital image correlation. Individual tests were modeled using finite elements, and the dynamic stiffness of the elastomer was identified by matching the simulation results with test data using numerical optimization. Using this method, the average dynamic response was found to be nearly equivalent to the quasi-static response measured with stress–strain curves at compressive strains up to 60%, with an uncertainty of $\pm 18\%$. Moreover, the behavior was consistent with the results in stress relaxation experiments and oscillatory tests although the latter were performed at lower strain levels.

Published by Elsevier Ltd.

1. Introduction

Tissue simulant materials are sought to provide realistic experimental devices to simulate the human body's response to blast or impact loading that can occur in military scenarios, law enforcement and emergency response events, vehicle accidents or sporting events (Roberts et al., 2007). This approach is meant to help develop better protective equipment or procedures to prevent serious injury or death. In practical injury scenarios, tissues are subject to dynamic loading involving large amplitude strains, generally in excess of 20% (Prange and Margulies, 2002)

to vulnerable soft tissues at strain rates above 10 s^{-1} (LaPlaca et al., 2005). Numerical models of these test devices are crucial to interpreting the measurement data obtained from these complicated tests, and efforts are underway to provide the material data needed to calibrate such models. Simpler uniaxial mechanical tests of soft tissue specimens show that the large-strain response of these materials is generally non-linear and rubber-like, and can be represented by hyperelastic models (Fung, 1993; Prange and Margulies, 2002; Roan and Vemaganti, 2007). Strain rate sensitivity is also generally observed in soft tissues, prompting the use of viscoelastic models to describe the

*Corresponding author. Tel.: +1 301 975 8114; fax: +1 301 975 4553.
E-mail address: smates@nist.gov (S.P. Mates).

relaxation behavior (Edsberg et al., 1999; Prange and Margulies, 2002; Sparks and Dupaix, 2008).

High strain rate measurements of actual tissues and tissue simulants are often performed using a Split Hopkinson Pressure Bar, or Kolsky Bar (Chen et al., 2002; Saraf et al., 2007a, 2007b), which can achieve large strains at uniform strain rates in excess of 100 s^{-1} . The difficulties in obtaining valid high strain rate data on soft materials using Kolsky bar techniques are well documented. Soft materials take much longer to achieve mechanical equilibrium when subject to a rapidly changing load. In most practical situations, equilibrium is not established in the sample until the test is nearly over, invalidating most if not all of the test (Chen et al., 2002). Careful selection of specimen thickness and the use of pulse shaping to increase the rise time of the load pulse have been effective methods for achieving valid dynamic test results (Song and Chen, 2004). Measuring the forces on soft samples is also challenging because they are below the typical sensitivity of Kolsky bars designed for testing metals. Special, highly sensitive force transducers placed directly on either side of the sample are required to obtain force signals (Casem et al., 2005). Care must be taken to separate out inertial effects in these force signals to obtain the true specimen response (Song et al., 2007). Finally, confinement techniques have been successfully employed to force either hydrostatic or shear loading conditions at high strain rates (Saraf et al., 2007a, 2007b).

For extremely soft materials (less than 10 Shore A), such as the material examined in our experiments, achieving force equilibrium in a Kolsky bar test is exceedingly difficult. Further, friction between the sample and the compression platens is difficult to eliminate, even with generous lubrication. Under dynamic loading, these effects will tend to produce non-uniform deformation in the sample in the form of large amplitude surface waves and prominent barreling. This behavior violates the requirements of uniform, uniaxial stress and strain throughout the specimen needed for valid dynamic measurements. In quasi-static compression tests, the effect of friction on the perceived stress-strain behavior can be significant. This has led some researchers to impose no-slip boundary conditions in order to more accurately determine the material response with a known, rather than ambiguous, state of friction (Miller, 2005; Roan and Vemaganti, 2007).

Recent advances in optical shape measurement using stereoscopic (3D) Digital Image Correlation (DIC) (Sutton et al., 2009) and in high speed digital camera technology has now made it feasible to measure the shape evolution of soft specimens during dynamic testing in a Kolsky bar. Further, by combining this new measurement capability with finite element modeling, the constitutive behavior of the material may be deduced in high rate tests using so-called inverse methods (Avril et al., 2008). Such methods, which can involve minimizing the difference between finite element simulations and experimental data by adjusting the relevant material parameters has been used to identify the properties of metals (Mahnken, 2000; Hoc et al., 2003; Cooreman et al., 2008), composites (Roux and Hild, 2008), ceramics (Robert et al., 2007), polymers (Giton et al., 2006) and biomaterials (Kauer et al., 2002) usually under equilibrium test conditions but more recently at high rates of strain (Kajberg and Wikman, 2007). The advance offered by this technique is to allow one to analyze tests where the stresses and strains are not uniform, which is relevant

to all situations of practical interest but until now has been beyond the capability of the majority of engineering test methods. In the present case, the benefits of the approach are that potential errors due to the usual assumption of frictionless conditions are avoided, and special specimen designs required to minimize inertial effects and specimen equilibrium are not needed. These considerable benefits come at the expense of higher equipment costs and the need for significant numerical analysis.

In this paper, high-speed 3D DIC is used to measure the dynamic deformation of a soft elastomer during high strain rate compression tests carried out with a Kolsky bar. A modified Kolsky bar technique is used here that employs a flying compression platen that detaches from the incident bar to allow much greater compressive strains in the specimen than otherwise possible. The sample is allowed to deform non-uniformly due to inertial effects and friction. Finite element modeling is employed to deduce the constitutive behavior of the material by matching the DIC shape history data and force history data recorded by force transducers. First, the sensitivity of the finite element model to the relevant physical parameters is analyzed. Then, optimal parameter values are identified by finding minima in the residual functions that numerically compare the simulation results to the data. The identified optimal parameters are averaged for five individual experiments and the result is then compared to the quasi-static behavior to determine the rate sensitivity of the material. Standard deviations of the identified parameters are used to estimate the overall uncertainty of the identified dynamic response of the specimen.

2. Experimental methods

The elastomer was cast into 9.5 mm diameter by 6.5 mm thick cylinders for compression testing. The material has a density of 870 kg/m^3 , and it is nearly transparent. Tests were conducted using a maraging steel Kolsky bar measuring 15 mm in diameter with 1500 mm long bars. Force measurements were made with piezo-electric dynamic force transducers placed on either side of the specimen, as shown in Fig. 1a. The force transducers have a resolution of $\pm 0.5 \text{ N}$ on the incident side and $\pm 0.25 \text{ N}$ on the transmission side. Polished steel platens (15 mm diameter by 5 mm thick) are placed between the transducers and the sample. No lubrication was used. The maraging steel striker bar is 250 mm long and 15 mm diameter and impacts the incident bar at approximately 5.5 m/s.

An additional difference between these tests and more traditional Kolsky bar testing is that the upstream platen and force transducer are allowed to collectively decouple from the incident bar and become a “flyer.” The flyer has the advantage of producing a much larger dynamic strain in the specimen than a normal Kolsky bar test, which is limited by the duration of the compressive pulse generated by the striker impact. This striker impact pulse is limited by the length the striker bar, which is typically no more than one quarter of the length of the incident bar. Thus, in normal Kolsky bar tests, the maximum available displacement (strain) is limited by the physical dimensions of the apparatus itself, for a fixed specimen size. Allowing the

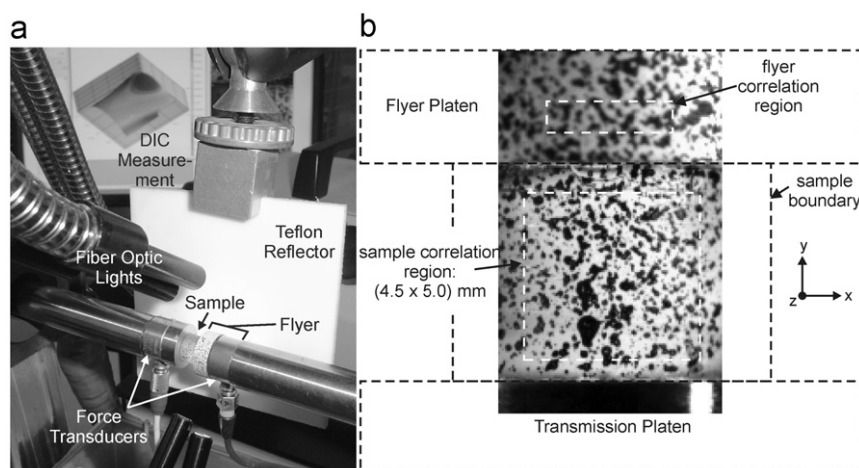


Fig. 1 – Experimental set-up. (a) Lighting arrangement. (b) DIC correlation regions on flyer and sample, and orientation.

upstream platen to separate from the incident bar eliminates this restriction by no longer limiting the sample compression to the length of the striker impact pulse. The flyer release was accomplished by using a low-tack adhesive at the incident bar-transducer interface that was strong enough to hold the pieces in place prior to the test but too weak to resist the strong tensile reflections of the incident wave off the platen-specimen interface. A soft pulse shaper (buna rubber, 5.5 mm diameter by 2.0 mm thick) was employed to produce a long, gradually rising stress pulse, which facilitated a repeatable flyer release. The alignment of the flyer during its flight was monitored by measuring its velocity vector with the DIC instrument. Data were ignored after the flyer deviated significantly from the orientation it had just after separating from the incident bar.

The DIC measurements were computed from stereo image pairs acquired at 120,000 frames per second with an image size of (128×128) pixels. Commercial DIC software¹ (<http://www.correlatedsolutions.com>, 2011) was used to perform image correlation measurements. The cameras used 90 mm macro (1:1 magnification) lenses with $f/5.6$ apertures and were placed 30 cm from the sample with a 12.5° pan angle, resulting in a resolution of 18 pixels/mm. A random speckle pattern was created on the samples using a light dusting of flat black spray paint. Attempts were made to achieve a nominal average speckle size of between 5 pixels and 7 pixels in diameter and a coverage factor of 50% following the software manufacturer's recommendations. However, in practice the speckles were often coarser than recommended, and the coverage factor was variable. Nevertheless, good correlation performance was routinely achieved. The speckle patterns were backlit using a Teflon reflector placed directly behind the specimen and illuminated by halogen optical fiber lamps, as shown in Fig. 1a. Fig. 1b indicates the typical correlation region obtained on the specimen and on the flyer. Correlation measurements used the default software analysis settings (21 pixel windowing, 5 pixel overlap, with default smoothing). The DIC measurement data, obtained from about 200 stereo image pairs during a typical test, were automatically oriented to a reference plane that is defined by fitting the initial shape of the (cylindrical) specimen prior to deformation. Because of this automatic plane fit and the fact that the sample deforms axisymmetrically, the DIC coordinate system could be aligned

with the axisymmetric finite element model coordinate system using simple y - and z -translations.

To explore the accuracy of the DIC displacement measurements, rigid glass cylinders of known dimensions were coated with a speckle pattern similar to the elastomer specimens and measured while undergoing translations. The initial plan was to measure the deforming specimens by fitting the radius of curvature of the DIC surface data along the length of the specimen, which would make maximal use of the data and could potentially identify if and when the sample deformation becomes no longer axisymmetric. To check the DIC accuracy in measuring radius of curvature, the shape of the stationary glass cylinders were measured and compared to the known radius of the glass cylinder. The average radius measured by DIC was 6.01 mm, or 6.6% below the actual cylinder radius of 6.43 mm. Fig. 2 demonstrates that the fit radius is less accurate and noisier than the out-of-plane position data along the center of the correlation region. Because of this, the out-of-plane (Z) position data along the center of the correlation region were chosen to compare with the simulated sample displacements rather than the radius of curvature computed by fitting the full 3D data set. Finally, the translation experiments indicated an accuracy of rigid body motion measurements was ± 0.01 mm. Noise levels were ± 0.001 mm, as determined by analyzing repeated exposures with no translation.

3. Calculation

The finite element model consists of the flyer assembly (force transducer plus steel platen), the sample, the transmitted force transducer and platen, and the transmission bar. ABAQUS/Explicit¹ is used to perform the simulations. A portion of the modeled mesh is shown in Fig. 3. The model uses axisymmetric CAX4R elements. The sample is modeled

¹ Commercial products are identified in this work to adequately specify certain procedures. In no case does such identification imply recommendation or endorsement by NIST, nor does it imply that the materials or equipment identified are necessarily the best available for the purpose.

with 352 elements, while the elastic force transducers, platens and bars are modeled with a much coarser mesh to reduce computation time. The mesh density provided good sample shape resolution and contact behavior while keeping the computation time short (about 1 min) on a quad-core desktop computer to enable many simulations to be run in a reasonable time. Time stepping is controlled automatically using the element-by-element option. Contact between the compression bars and the sample is modeled using the kinematic hard contact formulation. The maraging steel compression bars as well as the platens are modeled as linear elastic solids with the following properties: $E=1.9 \times 10^{11}$ Pa, $\nu=0.29$, and $\rho=8048$ kg/m³. The force transducers are modeled with the same stiffness and Poisson ratio as the maraging steel but with a density of 6594 kg/m³. The boundary conditions for the simulations of each individual experiment are set by specifying the velocity history of the flyer, which is obtained directly from DIC measurements in each test. This method assures correct time synchronization between the DIC data and the model and the exact gross deformation of the sample. Further, because each test is modeled individually, any variations due to small differences in the flyer velocity history (inertial effects) are captured by

the model. Simulations are carried out until the flyer velocity vector begins to deviate from the compression axis due to pitching, which occurs eventually when the flyer decelerates and comes to rest against the specimen.

The elastomer is modeled as an isotropic hyper-elastic material using the Marlow strain energy potential. Hyper-elasticity is characterized by large, recoverable elastic strains that are characteristic of rubbery materials. Rubbery response in polymeric materials occurs in the region nestled between the visco-elastic response and viscous flow region in strain-rate space (Ward and Hadley, 1993). Rubbery deformation behavior is governed by configurational entropy changes that occur as the long-chain polymeric molecules are reversibly stretched or compressed (Treloar, 1975). Micromechanical behavior associated with rate-dependency and dissipation, such as chain slippage and the breakage and reforming of secondary (cross-link) bonds, are less important in the rubbery regime. Experimental evidence suggests that for large strains, the response of rubbers can be rate-sensitive (Bergström and Boyce, 1998), owing to a dual-network of polymer chains, one that is characterized as perfectly hyper-elastic (rate-insensitive) and another that exhibits relaxation effects. This second network can exist as non-cross-linked “free chains” or the free ends of cross-linked chains (Treloar, 1975). Models proposed for this behavior are based on parallel arrangement of hyperelastic and viscoelastic concepts.

For present purposes, however, the rate-insensitive hyper-elastic material model is used initially to identify whether or not the elastomer of interest here exhibits significant rate sensitivity by comparing its dynamic response to its quasi-static behavior. If rate sensitivity is indicated by this comparison, an alternate material model, likely based on dual hyperelastic-viscoelastic approach as in Bergström and Boyce (1998), would then be employed to describe the material response over a range of strain rates. The baseline constitutive response of the material used in the model is derived from uniaxial stress-strain data obtained at a low strain rate (3.1×10^{-2} s⁻¹). The quasi-static response is shown in Fig. 4. To allow for possible rate effects, the response of the specimen is modified by a stiffness scaling factor, m :

$$m = \frac{E_{a,dyn}}{E_{a,qs}} \quad (1)$$

Here $E_{a,qs}$ is the apparent quasi-static modulus and $E_{a,dyn} = mE_{a,qs}$ is the apparent dynamic modulus identified here. Stress-strain curves for various values of m are plotted in

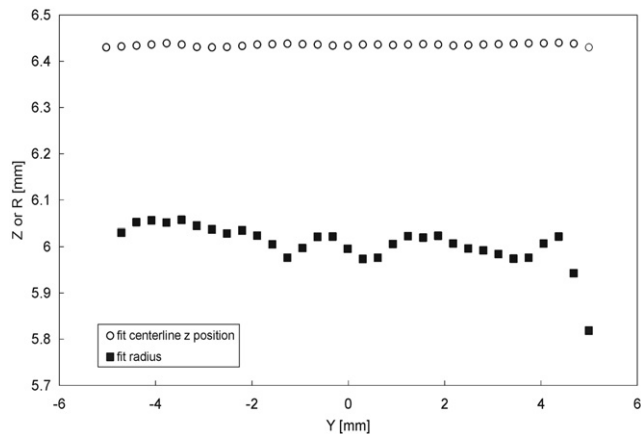


Fig. 2 – DIC measurement of the radius of a rigid glass cylinder (6.43 mm diameter) obtained by fitting the full 3D data set (fit radius, R) compared to the fit centerline z position obtained from the central portion (y-axis) of the DIC correlation region.

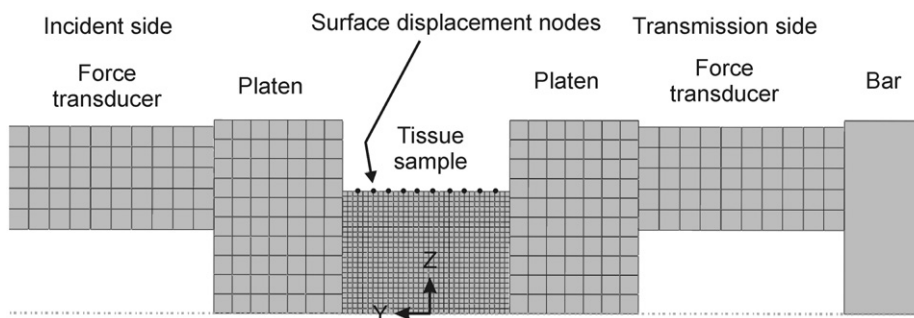


Fig. 3 – Axisymmetric finite element model showing the arrangement of the sample, platens, load cells and a portion of the transmission bar.

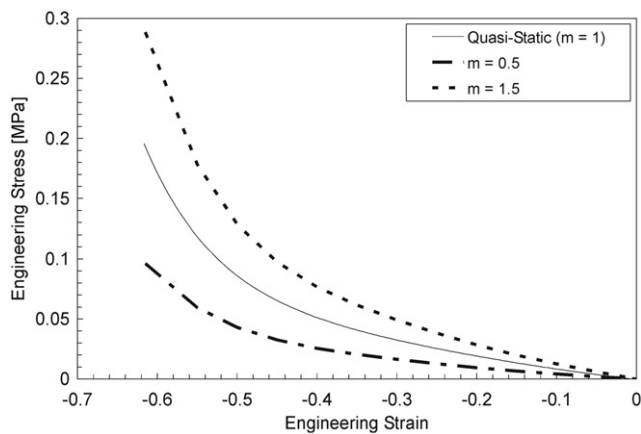


Fig. 4 – Quasi-static compression stress–strain response of tissue simulat with polynomial fit and two alternate models with twice ($m=2$) and half ($m=0.5$) the stiffness of the quasi-static response ($m=1$).

Fig. 4. Quasi-static behavior corresponds to $m=1$, while a stiffer response implies $m>1$ and a softer response implies $m<1$. In this study, m is varied to obtain the best possible agreement with the dynamic test data. In order to measure the strain and temperature sensitivity of this material, the apparent modulus was calculated using rubber elasticity theory (Ferry, 1980) from uniaxial stress–strain data and stress relaxation measurements. In addition, shear results were obtained using dynamic oscillation in torsion. These measurements, which were conducted at longer time scales than those experienced in the Kolsky bar, were conducted on cylindrical samples with an l/d that ranged from 0.33 to 0.66, where l is length and d is diameter. Note that in the finite element calculations, the factor m is used to modify baseline data in the inverse analysis, and fits to the data are not involved. Fitting of quasi-static, stress relaxation or oscillatory results is done after the analysis and is for the sole purpose of comparing the static behavior with the identified dynamic response.

Rubber-like materials, especially unfilled polymers, have a large bulk modulus relative to their shear modulus, such that Poisson's ratio is very close to 0.5. In an unconfined compression loading arrangement such as that used here, one expects very little measurable compressibility. However, the explicit finite element method employed requires a small amount of compressibility to work effectively (Dassault Systèmes, 2011a). A numerical study is used to select the most appropriate value based on computation costs and accuracy, as will be described shortly. In addition, a Coulomb friction model is used between the specimen and the compression platens. In this model, the shear stress necessary for slip equals the friction coefficient, f , multiplied by the normal contact pressure.

Finally, Rayleigh material damping is employed in the numerical scheme to eliminate unphysical oscillations in the simulations to better mimic the dynamic response of the sample. This method is used in the finite element code as a generic means to account for dissipation in many different materials (Dassault Systèmes, 2011a). It works by adding a small damping stress, σ_d , to the stress from the basic

hyperelastic response that is proportional to the strain rate $\dot{\epsilon}$ and modulus (E) by specifying a positive damping factor β :

$$\beta = \frac{\sigma_d}{E\dot{\epsilon}} \quad (2)$$

The magnitude of the damping factor must be chosen with caution as it is not intended to simulate the strain rate effects on the bulk micromechanical response of the specimen. Those effects will be manifest through changes in the strain energy potential, which would involve a change to the stress–strain curve (e.g. the value of m). To avoid obscuring strain-rate stiffening effects from those related to numerical damping, a minimal damping coefficient must be chosen that is just large enough to eliminate non-physical oscillations while not adding significant numerical stiffness to the sample.

A commercial software package (Dassault Systèmes, 2011b)¹ is used to perform the model sensitivity analysis and to identify the dynamic sample stiffness by comparing the simulation results to the experimental data. The software acts as GUI-driven macro that alters finite element model input data, controls the solver execution and displays and analyses the simulation results. It also approximates the finite element model response over the variable space of interest using interpolation functions, and employs a variety of optimization tools to search for optimal parameter values using objective functions that describe the agreement between the simulation results and the data. The objective functions are described next.

3.1. Objective functions

Objective functions expressing the difference between the finite element model results and the data are built individually for the force history and shape history data. Then, a single “cost” function is assembled to represent the overall agreement between simulation and data for identifying optimum parameter values. DIC shape history data are compared to the displacements of the surface nodes of the modeled specimens as indicated in Fig. 3. Residuals are computed at the DIC measurement locations along the center of the correlation region parallel to the compression (y -) axis at each measurement time point (e.g. for each image pair acquired and analyzed). The modeled surface positions are interpolated to match the DIC measurement positions along the length of the specimen. The shape history objective function, ϕ_s , is given by

$$\phi_s = \frac{1}{M} \sum_{t=1}^M \left\{ \frac{1}{N} \sum_{i=1}^N \left(\left[\frac{Z_{i,t}^{FEA} - Z_{i,t}^{DIC}}{Z_{i,t}^{DIC}} \right]^2 \right)^{0.5} \right\} \quad (3)$$

In Eq. (3), Z is the out-of-plane surface position of the deforming sample. The superscript FEA refers to the finite element model result, while the superscript DIC denotes experimental data (DIC measurement). ϕ_s is summed over space (index i) then time (index t) and divided by the total number of measurement points MN . The number of measurement points varies slightly from experiment to experiment. ϕ_s is computed using an in-house developed code that extracts $Z_{i,t}^{DIC}$ data from the DIC measurement files and the modeled surface node positions, $Z_{i,t}^{FEA}$, from the simulation results files, and performs spline interpolations on the

Table 1 – Estimated uncertainty in the objective function due to measurement resolution limits.

Shape	$\delta Z_{DIC}=0.00001$ m	$Z_{DIC}=0.00475$ m	NM=1000	$\delta\Phi_S=0.002$ m	$SF_S=0.001$
Force		$\delta F_{EXP}=0.25$ N	P=200	$\delta\Phi_F=50$ N	$SF_F=1000$
Total					$\delta\Phi=2.0$

simulated surface positions. This shape residual calculation method admits the possibility that the two data sets being compared do not cover the same range of y-values. In these cases, Z^{FEA} can be undefined at the non-overlapping end. To avoid unrealistically large residuals resulting from extrapolating the spline fit outside its defined range, these points are not considered in the residual sum. This will tend to reduce the sensitivity of the shape residual function to large discrepancies in the length of the sample between the model and the data, but this is not an issue when the discrepancies between the simulated and measured shape are small.

The transmitted force history objective function, Φ_F , is given by

$$\Phi_F = \sum_{j=1}^P ((F_j^{FEA} - F_j^{EXP})^2)^{0.5} \quad (4)$$

In Eq. (4), F is the transmission force. The superscripts EXP refers to the experimental data obtained from the force transducer, while FEA is again simulation results. Φ_F is summed over time only (using a different time index than the DIC data) to arrive at a single residual value representing the discrepancy between the data and each simulation run over the whole experiment. At each time step, Φ_F is calculated by linearly interpolating F^{FEA} at the time points where F^{EXP} is available. The calculation is performed using an optional plugin module within the commercial software used here to evaluate the objective functions that does not provide for normalization (Dassault Systèmes, 2011b)¹.

The combined objective function is assembled as follows:

$$\Phi = \frac{\Phi_F}{SF_F} + \frac{\Phi_S}{SF_S} \quad (5)$$

In Eq. (5), SF_F and SF_S are scale factors for the force and shape residuals, respectively. The scale factors are selected to weight each individual objective function such that the order of the scaled objective is near unity near the optimum point. For this study, $SF_F=1000$ N and $SF_S=0.001$.

A simple error estimate for Φ_S is based on constant values of measured and modeled values of the surface position Z :

$$\delta\Phi_S = \frac{Z^{FEA}}{(Z^{DIC})^2} \delta Z^{DIC} \quad (6)$$

With this method, differences in the uncertainties in the individual measured DIC displacements are disregarded, and all points are weighted equally, unlike Kajberg and Wikman (2007). The uncertainty in Φ_F due to an uncertainty δF^{EXP} on the experimental data, for constant values of F^{EXP} and F^{FEA} , is $\delta\Phi_F = P\delta F^{EXP}$ (7)

In the above equation, the uncertainty increases in proportion to the number of terms in the sum, such that more observations lead to a larger uncertainty, which is a consequence of the summation in the force residual equation. That the force residuals are not normalized (because they are

generated by commercial software with limited built-in options) is of no concern because the force and shape residuals are combined using additional scaling factors into $\delta\Phi$:

$$\delta\Phi = \sqrt{\left(\frac{\delta\Phi_F}{SF_F}\right)^2 + \left(\frac{\delta\Phi_S}{SF_S}\right)^2} \quad (8)$$

Table 1 lists estimates of the uncertainties for Φ_S , Φ_F and Φ based on nominal measurement resolutions of the DIC system and the force transducers. As the table shows, the total objective function uncertainty is dominated by the uncertainty in the DIC data. These uncertainties will be compared to the actual scatter in the identified values of m from repeat experiments. Sources of experimental and modeling errors are discussed in Results.

4. Results and discussion

Force-time data from a typical experiment are shown in Fig. 5 along with a sketch showing the corresponding behavior of the flyer plate during the test. Prominent features of the data are labeled in the graph. A sharp rise in the incident force marks the arrival of the incident compressive strain wave generated by the striker. As this wave reflects from the incident platen-sample interface, a tensile (negative) force is observed. This tensile load causes the flyer to break free from the incident bar and compress the specimen. As the specimen becomes more compressed, the transmitted force steadily increases, until the flyer arrests completely. At arrest, the transmitted force comes to a peak. Then, the strain energy that has been stored up in the sample due to the compression begins to release, causing the sample to push back on the flyer, resulting in a rapidly dropping force signal. Eventually the flyer runs back into the incident bar, which has been steadily advancing due to the ringing action of incident wave that remains trapped within it. This second impact is marked by the final sudden rise in both force signals.

Fig. 6 plots the overall sample strain and strain-rate versus time for the same experiment shown in Fig. 5. About 70% engineering strain is achieved before symmetry breaks down. Symmetry in the test is indicated by the flyer velocity orientation angle, also shown in Fig. 6, which is the cosine of the angle between the current velocity vector and the original compression axis as determined from the DIC measurements. To achieve this level of strain in the sample without the flyer technique, a Kolsky bar 10 times as long as the one used here would be needed. A second observation is that the strain rate is relatively uniform over most of the test. A constant strain rate is critical for a normal Kolsky bar test. Here, however, because an inverse analysis is used to

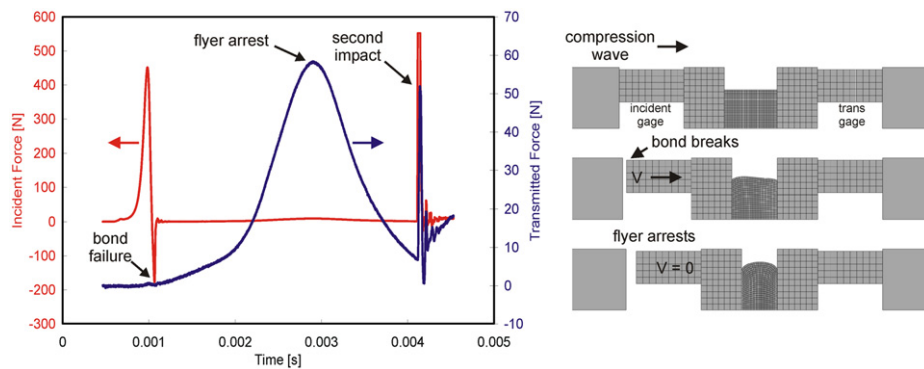


Fig. 5 – Force signals recorded on the incident and transmitted side of the specimen during a flyer experiment (left) and a sketch of the flyer experiment as visualized with an axisymmetric finite element simulation (right).

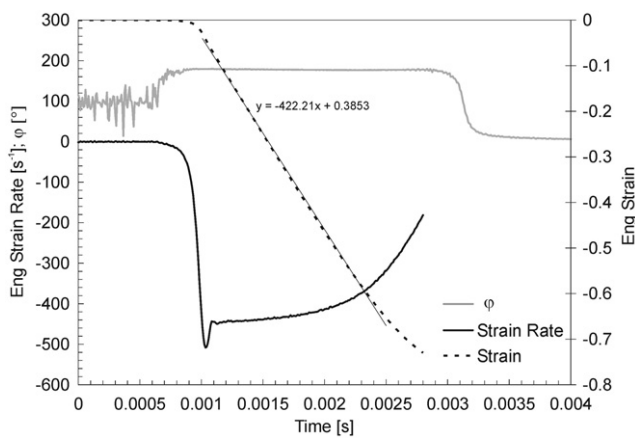


Fig. 6 – Flyer velocity orientation angle (ϕ), engineering strain rate and engineering strain history measured by DIC.

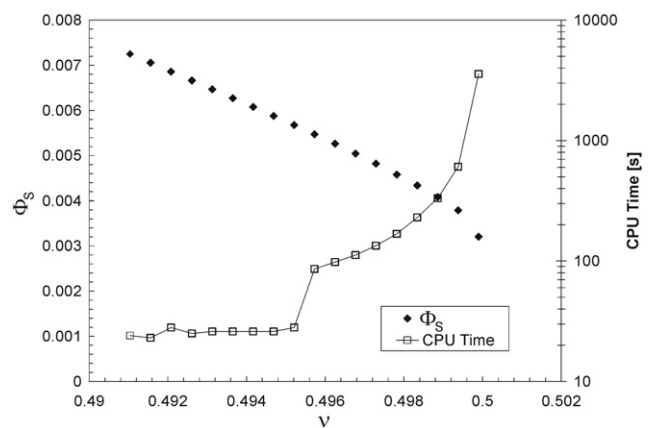


Fig. 7 – Influence of Poisson's ratio (ν) on shape agreement (Φ_S), and CPU time.

deduce the specimen response, the assumption of a constant strain rate is not required.

The parameters governing the behavior of the sample during the simulated flyer test are the stiffness factor, m , the friction coefficient, f , Poisson's ratio, ν , and the damping factor, β . In principle, all of these factors can be examined simultaneously by conducting a sensitivity analysis using a large Design-of-Experiments (DOE) matrix. However, certain parameters can be specified ahead of time to reduce the number of unknowns in the problem. For example, since very soft polymeric materials are incompressible, $\nu=0.5$ should be prescribed. However, as discussed earlier, computational stability requires that some compressibility be added, which will affect accuracy of the solution of this highly confined compression test. Fig. 7 plots values of the shape objective function, Φ_S , and the computation time for ν ranging from 0.4900–0.4999. While there is a continual improvement in Φ_S as ν approaches 0.5000, computational costs begin to rise at 0.4950 and become drastic at 0.4999. The choice of $\nu=0.4950$ combines good accuracy with reasonably fast execution time. This value is also recommended by the software manufacturer for elastomers under highly confined conditions (Dassault Systèmes, 2011a). The penalty for allowing compressibility is an under-prediction of the out-of-plane deformation, which introduces a systematic error that limits the

minimum value of Φ_S that can be achieved. The consequences of this compromise are discussed later. The other parameter that must be prescribed is the damping factor, β . As already discussed, because β is a numerical damping factor with an ambiguous physical interpretation, its influence should be minimized in order to avoid adding significant artificial stiffness that would confound efforts to identify the rate sensitivity of the elastomer. A series of simulations showing the effect of damping coefficient on the simulated force data compared to typical force transducer output is shown in Fig. 8. Here $m=1$. Selecting $\beta=0.000025$ provides a realistic-looking force signal while having little overall effect on the force levels themselves. Using Eq. (1), this damping level adds a stress equal to about 1% of the zero-strain modulus of the material for a global strain rate of 400 s^{-1} . Fig. 8 also demonstrates the gross overall stiffening of the material that occurs when the damping factor is too high. The effect of the particular choice of β on the identified stiffness factor, m , is examined later.

With ν and β now fixed, we proceed to investigate the influence of the stiffness factor, m , and the friction coefficient, f . To this end, a Full-Factorial DOE is performed between $0.0 < f < 2.0$ and $0.75 < m < 1.25$ with 10 levels for each parameter. Their influence on Φ_F and Φ_S are shown in Fig. 9. These contour plots are generated using a Radial Basis

Function (RBF) approximation to the finite element response surface within the DOE parameter space. The RBF approach method provides good approximations for both smoothly varying functions as well as those containing sharp gradients (Hardy, 1971). This figure shows that the friction coefficient strongly influences both Φ_F and Φ_S for low values of f , but at higher values the sensitivity to friction coefficient is low. The sensitivity of Φ_F to friction drops above $f=0.3$, while friction affects Φ_S up to about $f=0.5$. Due to the overall lack of sensitivity above $f=0.5$, identifying an optimal friction coefficient from the present DOE results would be difficult and the result would likely be unreliable. Fortunately, the experimental friction coefficient lies somewhere within this region of insensitivity, such that choosing a large friction coefficient (above 0.5) gives the best agreement with the data, as indicated by Fig. 9. Consequently, the friction coefficient is set to the limiting no-slip case for the remaining simulations.

DOE's were executed for each experiment with $0.75 < m < 1.5$ to identify the dynamic stiffness of the specimen relative to its quasi-static response. The values of other parameters were fixed to values discussed previously, namely: $\beta = 0.000025$, $\nu = 0.495$ and no-slip friction. A representative plot of the effect of m on Φ_F and Φ_S is shown in Fig. 10. Both Φ_F and Φ_S have distinct minima, though not at the same value of m . A conclusion from the latter observation is that the model is not able to achieve perfect agreement

with experimental observations, leading to this tradeoff between shape and force agreement. Since neither objective has clear precedence, both will maintain approximately equal weighting by using the previously-defined scale factors. The DOE results are fit using an RBF approximation model prior to searching for minima, as before. A typical comparison of the RBF fit against the actual FEA results, also shown in Fig. 10, indicates very close agreement. A Downhill Simplex optimization method (Dassault Systèmes, 2011b) is used to identify optimum values of the stiffness using the force response function for five independent experiments. The results are listed in Table 2. The average stiffness factor was $m_{opt} = 1.05 \pm 0.18$, where the uncertainty represents two standard deviations. Thus, within the observed repeatability level and over the range of strain rates examined, the material is not strain rate sensitive, as $m = 1.0$ represents the quasi-static response.

The lack of strain sensitivity in this elastomer was investigated further through quasi-static (stress-strain), transient, and oscillatory mechanical testing at different strains and temperatures. The temperature dependence of the complex shear modulus was measured at small strains using a parallel plate geometry in oscillation on a torsion rheometer (Ares G2, TA Instruments) from 0.04 rad/s to 70 rad/s over a temperature range of 25 °C to -45 °C. The shear storage modulus

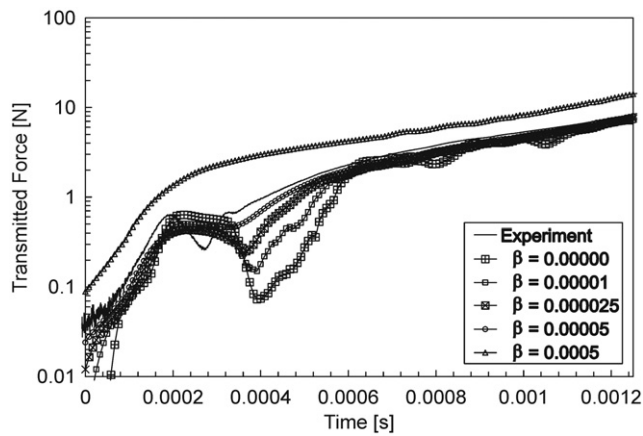


Fig. 8 - Effect of damping coefficient β on simulated transmitted force history compared with experiment.

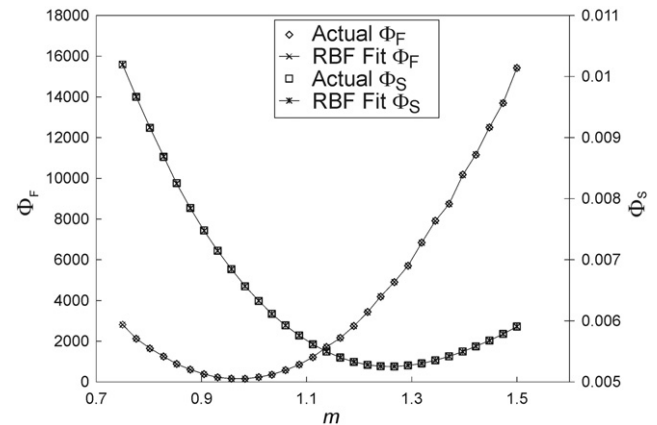


Fig. 10 - Effect of m on Φ_F and Φ_S along with the corresponding RBF approximations for the residual functions.

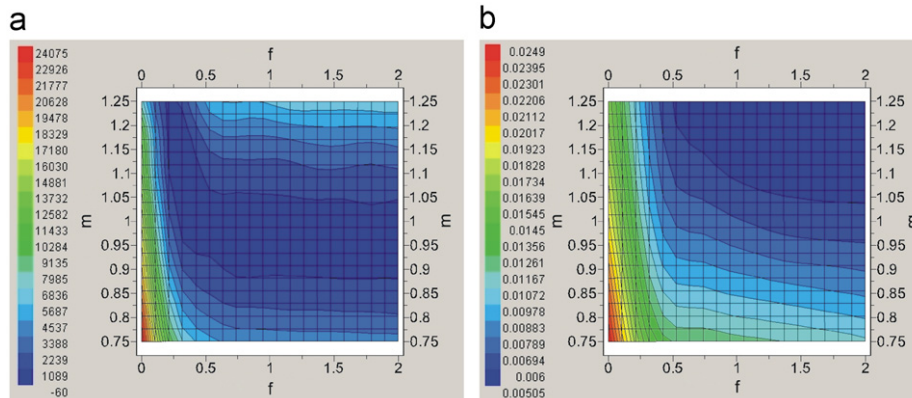


Fig. 9 - Effect of friction coefficient, f , and stiffness factor, m , on (a) Φ_F and (b) Φ_S .

Table 2 – Identified values of m_{opt} ($\beta=0.000025$, $\nu=0.495$, no-slip friction).

Experiment	Average strain rate [s^{-1}]	m_{opt}	$\Phi_{F,opt}$ [N]	$\Phi_{S,opt}$	Φ_{opt}
1	340	1.18	104	0.00623	6.33
2	397	1.04	475	0.00607	6.55
3	405	1.09	649	0.00573	6.38
4	429	0.94	1346	0.00686	8.20
5	422	1.02	897	0.00713	8.05
Average	399	1.05	694	0.0064	7.10
U^a	70	0.18	930	0.0012	1.86

^a U is the expanded uncertainty of the average value based on twice the standard deviation of the table values.

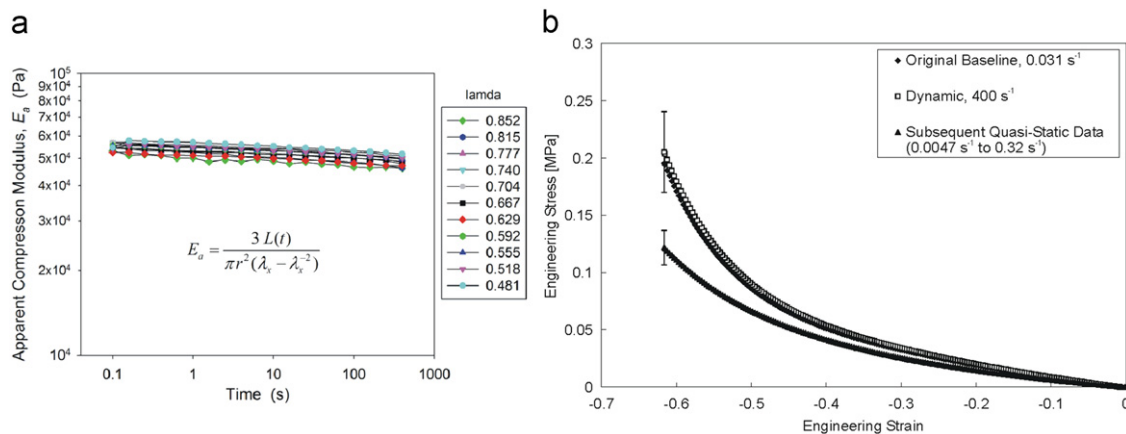


Fig. 11 – (a) Apparent compression modulus (E_a) derived from rubber elasticity theory utilizing stress relaxation experiments at increasing strain levels. (b) Additional uniaxial compression test data at strain rates between $0.0047 s^{-1}$ and $0.32 s^{-1}$ showing slightly softer response compared with the original baseline, which was found to contain a bias error. Error bars represent two standard deviations.

remained constant, $20 \text{ kPa} \pm 2 \text{ kPa}$, until approximately -10°C at which point it began to increase with decreasing temperature. In addition, the apparent compression modulus, $E_{a,qs}$, was measured using uniaxial stress–strain tests in compression and stress-relaxation measurements in compression. $E_{a,qs}$ was calculated from the Gaussian theory of rubberlike elasticity which has been used to calculate the equilibrium stress of a cross-linked polymer (Ferry, 1980). In stress relaxation experiments of soft solids under large deformations, this theory permits the separation of time dependence and strain dependence. The formula for $E_{a,qs}$ is

$$E_{a,qs}(t, \lambda) = \frac{3L(t)}{\pi r^2 (\lambda - \lambda^{-2})} \quad (9)$$

where L is load, r is the radius of cylinder, and λ is the extension ratio ($=\epsilon+1$, ϵ being the nominal stress). Fig. 11a plots $E_{a,qs}$ over 4 decades of time and a strain range from 0.15–0.52. The compression modulus over this large range of strain and time is $55 \text{ kPa} \pm 5 \text{ kPa}$. This close to, but somewhat softer than the apparent modulus calculated from uniaxial compression tests of $74 \text{ kPa} \pm 2 \text{ kPa}$ up to $\epsilon=0.58$. Given the fact that the Poisson's ratio of this elastomer is near 0.5, the apparent compression modulus is close to the measured shear storage modulus given by $E/3=20 \text{ kPa}$. While these measurements could not be shifted to cover the exact time scale of the Kolsky measurements, which are about two

orders of magnitude smaller, the lack of strain, time, and temperature difference supports the conclusion obtained from the inverse method that this elastomer is not highly rate sensitive over the range of strain rates investigated, even up to very large strains.

Because $E_{a,qs}$ determined from the stress-relaxation tests was found to be somewhat softer than the baseline quasi-static response used to identify the dynamic stiffness, additional stress–strain tests were performed in compression at strain rates between $0.0047 s^{-1}$ and $0.32 s^{-1}$. The data, which indicated no observable trend with strain rate, confirmed the slightly lower apparent modulus indicated by the stress-relaxation data. The original baseline data were affected by a bias error introduced into the determination of sample strain. The average of the additional quasi-static tests, equivalent to $E_{a,qs}=57 \text{ kPa} \pm 7 \text{ kPa}$, is plotted in Fig. 11b along with the original baseline quasi-static response and the identified apparent dynamic modulus of $E_{a,dyn}=80 \text{ kPa} \pm 10 \text{ kPa}$. Although the baseline response was slightly stiffer than the subsequent measurements indicated, within the estimated uncertainties, the rate sensitivity of this material between $0.0047 s^{-1}$ and $400 s^{-1}$ is quite small.

The 18% uncertainty in the identified m_{opt} reflects errors due to experimental and modeling approximation factors. These errors are now examined. Fig. 12 compares the simulated shape and force histories to experimental data at the optimal stiffness for Experiment 2 (see Table 2), which is typical of the

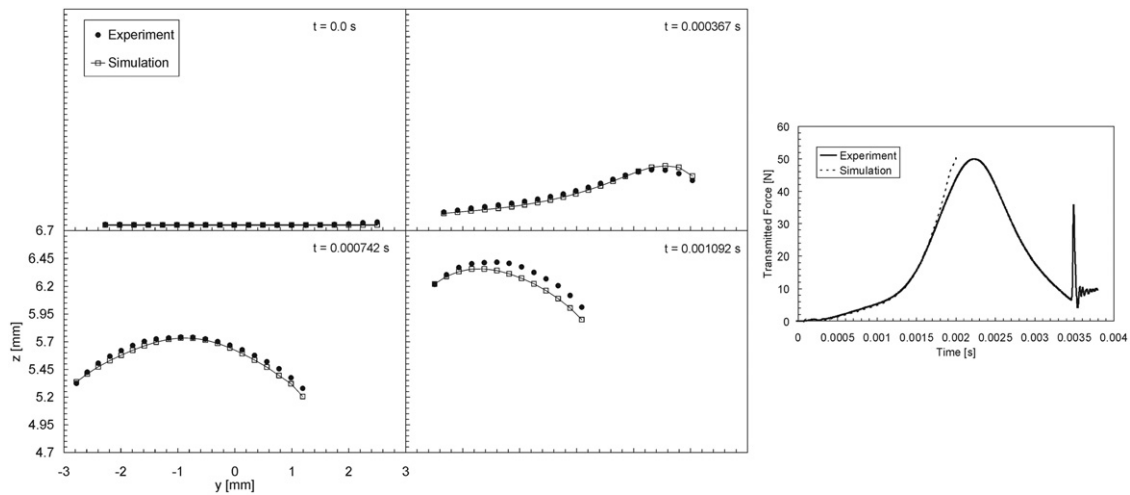


Fig. 12 – Comparison of simulation results and experimental data at the optimal stiffness (Experiment 2, $m_{opt}=1.04$).

Table 3 – Identified values of m_{opt} with $\beta=0.0001$.

Experiment	Average strain rate	m_{opt}	$\Phi_{F,opt}$ [N]	$\Phi_{S,opt}$	Φ_{opt}
1	340	1.03	30	0.00624	6.27
2	397	0.908	404	0.00522	5.62
3	405	0.947	531	0.00571	6.24
4	429	0.806	1149	0.00638	7.53
5	422	0.874	927	0.00713	8.06
AVG	399	0.92	608	0.0061	6.74
U^a	70	0.17	880	0.00144	2.00

^a U is the expanded uncertainty of the average value based on twice the standard deviation of the table values.

other tests. The overall agreement between the simulation and the data is excellent. As Table 2 indicates, with an average value of $\Phi_{S,opt}=0.0064$, the modeled shape is within 0.64% of the measured shape throughout all experiments. This amounts to about 0.03 mm, using Eq. (2) and using an average Z^{DIC} equal to half the maximum displacement in a typical experiment. Although excellent, this agreement is somewhat beyond the estimated 0.01 mm measurement resolution of the DIC system, and thus additional error is involved. As already discussed, a major contributor is the artificial compressibility in the model, which limits the sample deformation normal to the loading direction. This effect can be seen in Fig. 12, where the simulated sample has significantly less radial displacement than the experiment toward the end of the test. The average value of $\Phi_{F,opt}$ from Table 3 represents an average discrepancy between the force transducer measurement and the simulation of about 3 N (Eq. (3)), which is also larger than the inherent uncertainty of the measuring device (about 0.25 N). As Fig. 12 indicates, however, much of the force error occurs at the tail end of the experiment, where the flyer has slowed considerably and is more prone to tumbling. Exact concentricity of the specimen with the bars is also critical for perfect axisymmetry in the flyer motion, especially as the flyer approaches rest. That the standard deviation of $\Phi_{F,opt}$ is of the same order of magnitude as its value indicates there is no obvious systematic component to the force residual as was the case with the shape residual.

Because this elastomer is relatively strain rate insensitive over the range examined, the deformations and forces should be comparable at identical strains. Therefore, experimental scatter can be visualized by comparing the shape and force data at equivalent strains, which is done in Figs. 13 and 14. The shape data of Fig. 13 show a scatter of about 0.1 mm over the five tests, or about an order of magnitude larger than the instrument resolution uncertainty. However, much of this “scatter” is actually captured by the simulation, since the average difference between the model and the data is only about 0.03 mm. Thus much of the “scatter” in Fig. 13 is likely due to inertial effects which depend strongly on the imposed deformation velocity. Fig. 14 also indicates that, in general, higher flyer velocities (higher strain rates) correlate with larger transmitted forces. Additionally, the dynamic tests all show much larger transmitted forces than the quasistatic baseline response, which again is quite close to the identified dynamic response. It is interesting to consider that, had traditional Kolsky bar methods been used to analyze the force-deflection data, a much larger positive strain rate sensitivity would have been indicated.

Finally, it is noted that the identified value of m_{opt} depends on the particular choice of damping coefficient. Any attempt to “identify” an optimal m - β pair would be fruitless because of the similar effects these parameters have on force and shape, resulting in a continuum of acceptable solutions in m - β space. Had a larger value of β been chosen, a softer response would be identified because of the additional

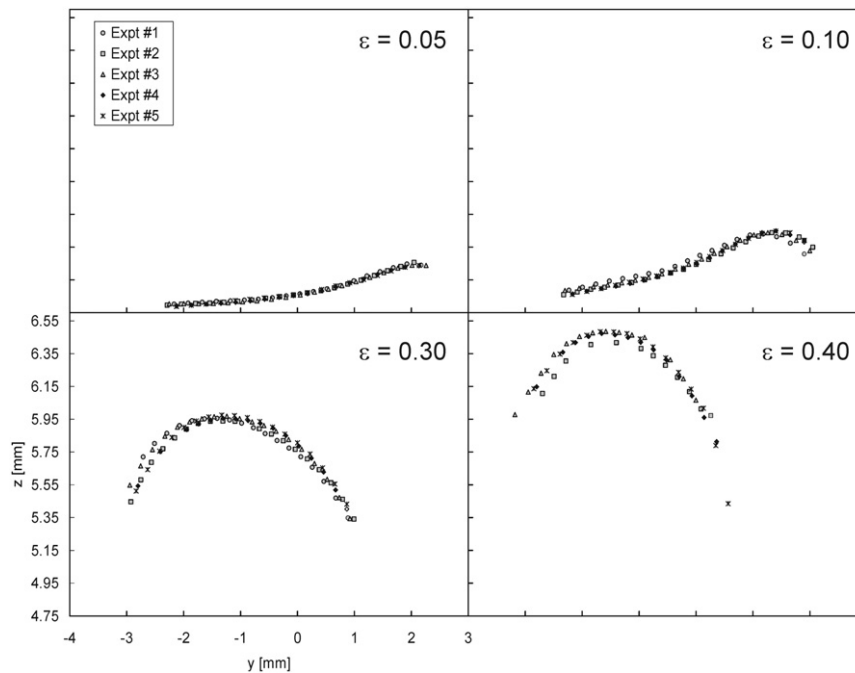


Fig. 13 – Shape data plotted at equivalent engineering strains for the five dynamic experiments used to evaluate m .

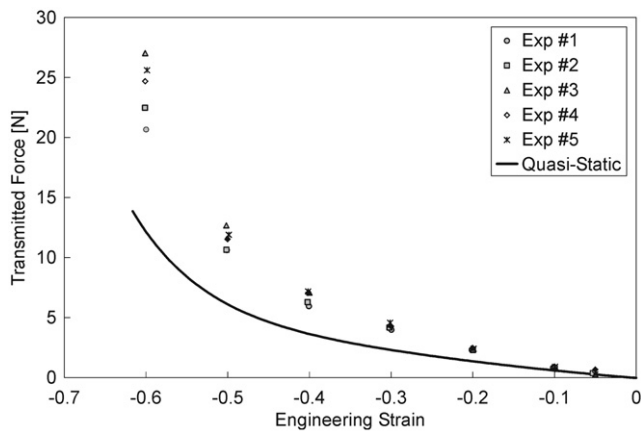


Fig. 14 – Force data plotted at equivalent engineering strains for the five dynamic experiments used to evaluate m , along with the original baseline quasi-static response (equivalent to the identified dynamic response).

artificial damping stiffness. For example, choosing an overdamped value such as $\beta=0.0001$ leads to a 13% reduction to $m_{opt}=0.91\pm 0.16$ ($k=2$), as shown in Table 3. It remains our contention, however, that β should be kept as small as possible since it does not have any distinct physical meaning but is rather numerical in nature. In neither case, however, does this elastomer exhibit strong rate sensitivity over the range of conditions examined here.

5. Conclusions

An inverse method was used to determine the dynamic stiffness of a prospective biomimetic elastomer using a

Kolsky bar to determine whether its strain rate sensitivity is similar what is reported for real soft tissues. This elastomer is intended for use in a human surrogate physical model to study tissue damage associated with concussive impacts. The inverse approach was used to avoid the common experimental difficulties that hinder dynamic testing of very soft materials, namely those related to friction and inertial effects. In addition, an unconventional flyer technique was used to extend the amount of compressive strain applied to the specimen beyond normal Kolsky bar methods to exceed the tissue damage threshold. High-speed digital image correlation (DIC) was used to capture the deformation history of the sample during dynamic testing, from the initial asymmetric transient period to the highly barreled final shape. A finite element model of the experiment was constructed and the resulting simulations were compared to the DIC shape history data and to force history data. The sensitivity of the model to specimen stiffness, friction, Poisson ratio and damping were examined, and the simulation results were compared to the experimental data to identify the dynamic stiffness using an inverse method. An appropriate numerical damping coefficient was chosen which produced realistic-looking force-history signals while avoiding adding artificial stiffness to the specimen that would confound attempts to identify a unique dynamic stiffness. Friction was modeled with a no-slip condition, which gave excellent agreement with the shape data. With friction and damping conditions established, optimal stiffness scale factors, m , were identified for each of five separate experiments. An average stiffness scale factor of $m_{opt}=1.05\pm 0.18$ was obtained, which is equivalent to a hyperelastic modulus of $80\text{ kPa}\pm 10\text{ kPa}$. Compared to the a stiffness of $57\text{ kPa}\pm 7\text{ kPa}$ from quasi-static (stress-strain) and stress-relaxation tests, this elastomer was found to be only weakly rate sensitive for compressive strains up to 60% and at strain rates between 0.031 s^{-1}

and 400 s^{-1} . Finally, this study shows how the inverse method can account for both friction and inertia effects, the latter of which would have indicated a much stronger positive strain rate sensitivity for this material had conventional Kolsky bar methods been used. However, numerical damping in the finite element model complicates efforts to identify a unique dynamic stiffness using this method.

Acknowledgments

The authors would like to thank Michael Kennedy of NIST and Christopher J. Kindle of NRL for their assistance in this work.

REFERENCES

- Avril, S., Bonnet, M., Bretelle, A.-S., Grédiac, M., Hild, F., Ienny, P., Latourte, F., Lemosse, D., Pagano, S., Pagnacco, E., Pierron, F., 2008. Overview of identification methods of mechanical parameters based on full-field measurements. *Experimental Mechanics* 48, 381–402.
- Bergström, J.S., Boyce, M.C., 1998. Constitutive modeling of the large strain time-dependent behavior of elastomers. *Journal of the Mechanics and Physics of Solids* 46, 931–954.
- Casem, D., Weerasooriya, T., Moy, P., 2005. Inertial effects in quartz force transducers embedded in a split Hopkinson pressure bar. *Experimental Mechanics* 45, 368–376.
- Chen, W., Lu, F., Frew, D.J., Forrestal, M.J., 2002. Dynamic compression testing of soft materials. *Journal of Applied Mechanics* 69, 214–223.
- Cooreman, S., Lecompte, D., Sol, H., Vantomme, J., Debruyne, D., 2008. Identification of mechanical material behavior through inverse modeling and DIC. *Experimental Mechanics* 48, 421–433.
- Correlated Solutions Inc., Columbia, SC, USA, <www.correlatedsolutions.com>, 2011.
- Dassault Systèmes, Vélizy-Villacoublay, France, <www.simulia.com/products/abaqus_explicit.html>, 2011a.
- Dassault Systèmes, Vélizy-Villacoublay, France, <www.simulia.com/products/isight.html>, 2011b.
- Edsberg, L.E., Mates, R.E., Baier, R.E., Lauren, M., 1999. Mechanical characteristics of human skin subjected to static versus cyclic normal pressures. *Journal of Rehabilitation Research and Development* 36, 1–9.
- Ferry, J.D., 1980. *Viscoelastic Properties of Polymers*. John Wiley & Sons Inc., New York.
- Fung, Y.C., 1993. *Biomechanics: Mechanical Properties of Living Tissues*. Springer-Verlag, New York.
- Giton, M., Caro-Bretelle, A.-S., Ienny, P., 2006. Hyperelastic behavior identification by a forward problem resolution: application to a tear test of a silicone-rubber. *Strain* 42, 291–297.
- Hardy, R.L., 1971. Multiquadratic equations of topography and other irregular surfaces. *Journal of Geophysical Research* 76, 1905–1915.
- Hoc, T., Crépin, J., Gélébart, L., Zaoui, A., 2003. A procedure for identifying the plastic behavior of single crystals from the local response of polycrystals. *Acta Materialia* 51, 5477–5488.
- Kajberg, J., Wikman, B., 2007. Viscoplastic parameter estimation by high strain-rate experiments and inverse modeling—Speckle measurements and high-speed photography. *International Journal of Solids and Structures* 22, 145–164.
- Kauer, M., Vuskovic, V., Dual, J., Szekely, G., Bajka, M., 2002. Inverse finite element characterization of soft tissues. *Medical Image Analysis* 6, 275–287.
- LaPlaca, M.C., Cullen, D.K., McLoughlin, J.J., Cargill, R.S., 2005. High rate shear strain of three-dimensional neural cell cultures: a new in vitro traumatic brain injury model. *Journal of Biomechanics* 38, 1093–1105.
- Mahnken, R., 2000. A comprehensive study of a multiplicative elastoplasticity model coupled to damage including parameter identification. *Computers and Structures* 74, 179–200.
- Miller, K., 2005. Method of testing very soft biological tissues in compression. *Journal of Biomechanics* 38, 153–158.
- Prange, M.T., Margulies, S.S., 2002. Regional, directional and age-dependent properties of the brain undergoing large deformation. *ASME Transactions: Journal of Biomechanical Engineering* 124, 244–252.
- Roan, E., Vemaganti, K., 2007. The nonlinear material properties of liver tissue determined from no-slip uniaxial compression experiments. *ASME Transactions: Journal of Biomechanical Engineering* 129, 450–456.
- Robert, L., Nazaret, F., Cutard, T., Orteu, J.-J., 2007. Use of 3D digital image correlation to characterize the mechanical behavior of a fiber reinforced refractory castable. *Experimental Mechanics* 47, 761–773.
- Roberts, J.C., Merkle, A.C., Biermann, P.J., Ward, E.E., Carkhuff, B.G., Cain, R.P., O'Connor, J.V., 2007. Computational and experimental models of the human torso for non-penetrating ballistic impact. *Experimental Mechanics* 40, 125–136.
- Roux, S., Hild, F., 2008. Digital Image Mechanical Identification (DIMI). *Experimental Mechanics* 48, 495–508.
- Saraf, H., Ramesh, K.T., Lennon, A.M., Merkle, A.C., Roberts, J.C., 2007a. Mechanical properties of soft human tissues under dynamic loading. *Journal of Biomechanics* 40, 1960–1967.
- Saraf, H., Ramesh, K.T., Lennon, A.M., Merkle, A.C., Roberts, J.C., 2007b. Measurement of dynamic bulk and shear response of soft human tissues. *Experimental Mechanics* 47, 439–449.
- Song, B., Chen, W., 2004. Dynamic stress equilibration in split Hopkinson pressure bar tests on soft materials. *Experimental Mechanics* 44, 300–312.
- Song, B., Ge, Y., Chen, W.W., Weerasooriya, T., 2007. Radial inertia effects in Kolsky bar testing of extra-soft specimens. *Experimental Mechanics* 47, 659–670.
- Sparks, J.L., Dupaix, R.B., 2008. Constitutive modeling of rate-dependent stress-strain behavior of human liver in blunt impact loading. *Annals of Biomedical Engineering* 36, 1883–1892.
- Sutton, M.A., Orteu, J.-J., Schreier, H.W., 2009. *Image Correlation for Shape, Motion and Deformation Measurements*. Springer Science+Business Media, New York.
- Treloar, L.R.G., 1975. *The Physics of Rubber Elasticity*. Clarendon Press, Oxford, England.
- Ward, I.M., Hadley, D.W., 1993. *An Introduction to the Mechanical Properties of Solid Polymers*. Wiley, Chichester, England.